RSC Advances

PAPER

View Article Online
View Journal | View Issue

Cite this: *RSC Adv.*, 2021, **11**, 26336

Tuning the microstructural and magnetic properties of $CoFe_2O_4/SiO_2$ nanocomposites by Cu^{2+} doping

Jie Hua,[ab] Zeyuan Cheng,[b] Zihang Chen,[b] He Dong,[ab] Peiding Li [b] and Jin Wang *[ab]

Received 20th June 2021
Accepted 26th July 2021

DOI: 10.1039/d1ra04763a

rsc.li/rsc-advances

Co–Cu ferrite is a promising functional material in many practical applications, and its physical properties can be tailored by changing its composition. In this work, $Co_{1-x}Cu_xFe_2O_4$ ($0 \leq x \leq 0.3$) nanoparticles (NPs) embedded in a SiO_2 matrix were prepared by a sol–gel method. The effect of a small Cu^{2+} doping content on their microstructure and magnetic properties was studied using XRD, TEM, Mössbauer spectroscopy, and VSM. It was found that single cubic $Co_{1-x}Cu_xFe_2O_4$ ferrite was formed in amorphous SiO_2 matrix. The average crystallite size of $Co_{1-x}Cu_xFe_2O_4$ increased from 18 to 36 nm as Cu^{2+} doping content x increased from 0 to 0.3. Mössbauer spectroscopy indicated that the occupancy of Cu^{2+} ions at the octahedral B sites led to a slight deformation of octahedral symmetry, and Cu^{2+}doping resulted in cation migration between octahedral A and tetrahedral B sites. With Cu^{2+} content increasing, the saturation magnetization (M_s) first increased, then tended to decrease, while the coercivity (H_c) decreased continuously, which was associated with the cation migration. The results suggest that the Cu^{2+} doping content in $Co_{1-x}Cu_xFe_2O_4$ NPs plays an important role in its magnetic properties.

1. Introduction

Cobalt ferrite ($CoFe_2O_4$) with moderate saturation magnetization, high coercivity and Curie temperature, as well as excellent chemical stability has gained increasing attention in technological applications, such as magnetic recording, catalysis, biotargeted drug delivery, magnetic resonance imaging, and spintronics.[1–7] In general, $CoFe_2O_4$ possesses a cubic inverse spinel structure with the $Fd\bar{3}m$ space group,in which Co^{2+} ions predominantly occupy octahedral B sites and Fe^{3+} ions are almost equally distributed between tetrahedral A and octahedral B sites. However, cation distribution between the A and B sites varies with the chemical composition and synthesis procedure. Designing the composition through the incorporation of divalent metal ions (such as Zn^{2+}, Mn^{2+}, Cu^{2+}, and Ni^{2+}) serves as a flexible strategy to tune the cation distribution of $CoFe_2O_4$ nanoparticles (NPs), which may be beneficial to further modify their physical properties or introduce novel functionalities.[8–10]

Recently Co–Cu ferrite, prepared through doping Cu^{2+} in $CoFe_2O_4$ NPs has been widely exploited for a variety of technological applications. Venkateshwarlu *et al.*[8] reported that the increasing Seebeck coefficient was observed in $CoFe_2O_4$ after doping with Cu^{2+} ions. The enhanced effect of Cu^{2+} doping on photocatalytic degradation efficiency of $CoFe_2O_4$ was reported by Sundararajan *et al.*[4] They also found that with Cu^{2+} content increasing, the saturation magnetization (M_s) decreased monotonously while the coercivity (H_c) first increased then decreased. Sanpo *et al.*[11] demonstrated the substitution of Cu^{2+} ions into $CoFe_2O_4$ could improve the antibacterial property on against multidrug-resistant *E. coli* and *Staphyloc occus aureus*. These experimental results suggest that Cu^{2+} doping content in $CoFe_2O_4$ significantly influences their physical property. However, it is well known that copper ferrite ($CuFe_2O_4$) can exist in face-centered cubic and face-centered tetragonal phases due to obvious Jahn–Teller distortion of Cu^{2+} ions.[13] Thus, when larger content of Cu^{2+} ions was doped in $CoFe_2O_4$ lattice, the crystal structure can transfer from cubic to tetragonal phase.[12–14] Balavijayalakshmi *et al.* have reported that as the Cu^{2+} doping content x was >0.6, tetragonal $CuFe_2O_4$ can be observed in cubic $Co_{1-x}Cu_xFe_2O_4$ NPs prepared by co-precipitation method.[12] With small content of Cu^{2+} ions doping in $CoFe_2O_4$ NPs, the crystal microstructure and physical properties can be tailored and investigated without undesired phase transformation. To date, a limited extent of work has been found in the literature on the microstructural investigation of Co–Cu ferrites with small Cu^{2+} doping content.

Magnetic $CoFe_2O_4$ NPs prepared by chemical method are prone to agglomerate, which makes it quite difficult to exploit their unique physical properties for practical applications. Two strategies have been developed to stabilize and reduce nanoparticle agglomeration, obtaining single phase ferrite. One is

[a]*Key Laboratory of Functional Materials Physics and Chemistry of the Ministry of Education, Jilin Normal University, Siping 136000, China. E-mail: jwang@jlnu.edu.cn*
[b]*College of Information Technology, Jilin Normal University, Siping 136000, China*

coating $CoFe_2O_4$ NPs with a uniform and stable ultrathin layer to form core–shell NPs. Since the thickness of the coating layer (such as ultrathin phosphate layer[15] and silicon carbide layer[16]) is only of a few nanometers, the magnetic properties of the $CoFe_2O_4$ core are not compromised after capping. The other is dispersing $CoFe_2O_4$ NPs in non-magnetic matrix to form nanocomposites, for example, dispersing $CoFe_2O_4$ in amorphous SiO_2, *i.e.* $CoFe_2O_4/SiO_2$ nanocomposites.[17–20] For SiO_2-based nanocomposites, SiO_2 network can not only provide spatial nucleation sites for $CoFe_2O_4$ NPs, promote the formation of single-phase spinel, but also minimize the surface roughness and spin disorder, thereby enhance the magnetic properties of nanocomposites.[21,22]

In this work, we prepared $Co_{1-x}Cu_xFe_2O_4/SiO_2$ nanocomposites ($0 \leq x \leq 0.3$) using sol–gel method, in which SiO_2 was used to obtain monophasic Co–Cu ferrites. With small amount Cu^{2+} ion doping, the crystal microstructure and physical properties were tailored without phase transformation. The goal of the present work is to study the effect of the small amount of Cu^{2+} doping on the microstructure, the hyperfine interaction, and magnetic properties of $Co_{1-x}Cu_xFe_2O_4$ by using X-ray diffractometer (XRD), Mössbauer spectroscopy, and vibrating sample magnetometer (VSM) at room temperature. The result shows that the crystallite size of $Co_{1-x}Cu_xFe_2O_4$ increases with Cu^{2+} content. The Cu^{2+} doping in $CoFe_2O_4$ induces a slight deformation of octahedral symmetry and change in cation distribution, which in turn modifies the values of M_s and H_c.

2. Experiments

2.1 Synthesis of $Co_{1-x}Cu_xFe_2O_4/SiO_2$ nanocomposites

The synthesis diagram for $Co_{1-x}Cu_xFe_2O_4/SiO_2$ nanocomposites (70% wt. ferrite/30% wt. SiO_2) is presented in Fig. 1. Using cobalt nitrate hexahydrate ($Co(NO_3)_2 \cdot 6H_2O$), ferric nitrate nonahydrate ($Fe(NO_3)_3 \cdot 9H_2O$), copper(II) nitrate trihydrate ($Cu(NO_3)_2 \cdot 3H_2O$) as iron, cobalt, and copper sources, and tetraethyl orthosilicate (TEOS) as precursor of SiO_2, a series of $Co_{1-x}Cu_xFe_2O_4/SiO_2$ nanocomposites ($x = 0$, 0.1, 0.2, and 0.3) were synthesized by sol–gel method. Firstly, the metal nitrates were weighted by the designed molar ratio and thoroughly dissolved in ethanol with magnetic stirring. Then, 1.5 mL ethylene glycol and 9.6 mL TEOS ethanol solution (volume ratio of 1 : 1) was injected into the solution, followed by adding 1 mL HNO_3 and continuously stirring for 5 h. Secondly, the solution was evaporated on a 60 °C water bath to form black brown sol. After that, the sol was dried at 100 °C for at least 24 h to form xerogel. Finally, the obtained gel was calcined at 1000 °C for 2 h in air and cooled to room temperature. The final collected product was taken for further investigation.

2.2 Characterization

The crystal structure, morphology, and magnetic properties of the as-prepared $Co_{1-x}Cu_xFe_2O_4/SiO_2$ were investigated by Rigaku D/max-2500 X-ray diffractometer (XRD, $\lambda = 1.5406$ Å), JEM-2100HR transmission electron microscope (TEM), and LakeShore7407 vibrating sample magnetometer (VSM, $B = 1.5$ T), respectively. The crystallite size of $Co_{1-x}Cu_xFe_2O_4$ was estimated by using Scherrer's formula. The room temperature Mössbauer spectra were collected on a FAST Comtec Mössbauer system in transmission mode, using a $^{57}Co(Pd)$ source and a conventional constant acceleration mode. The Mössbauer spectra of the samples were fitted using Lorentzian lines *via* the least square method.

3. Results and discussion

3.1 Structure and morphology analysis

XRD patterns of the as-prepared $Co_{1-x}Cu_xFe_2O_4/SiO_2$ samples are shown in Fig. 2. The diffraction peaks from (111), (220), (311), (222), (321), (400), (422) and (511) are consistent with the standard spectrum of cubic spinel $CoFe_2O_4$ (JCPDS no. 22-1086), which demonstrates the formation of Co–Cu ferrite with no detectable impurity phases. No reflection from SiO_2 can be

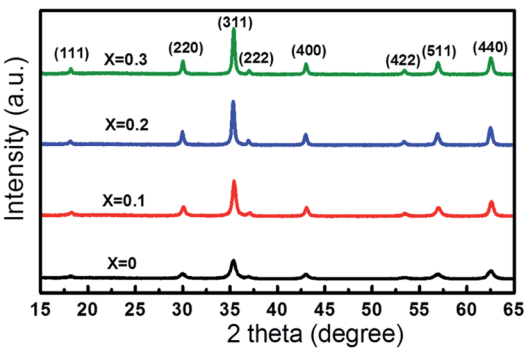

Fig. 2 XRD patterns of the as-synthesized $Co_{1-x}Cu_xFe_2O_4/SiO_2$ with different Cu^{2+} content.

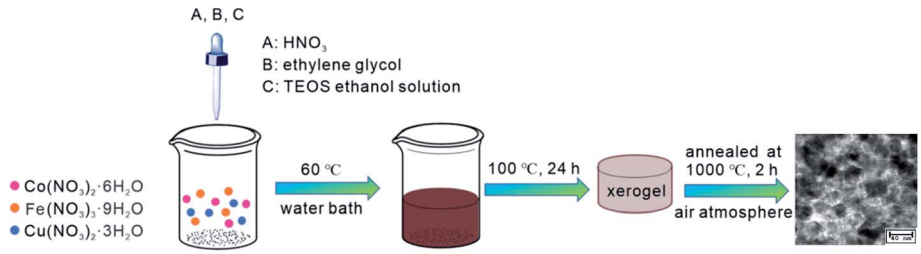

Fig. 1 Schematic diagram of the synthesis method for $Co_{1-x}Cu_xFe_2O_4/SiO_2$ nanocomposites.

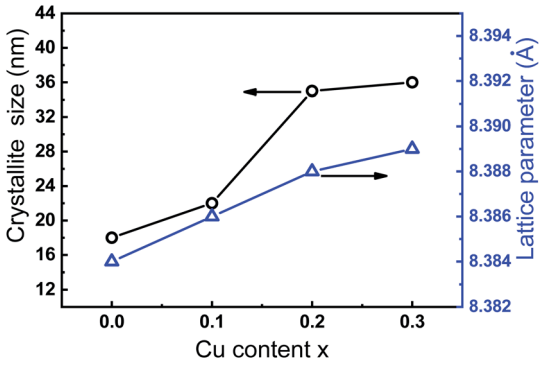

Fig. 3 Plot of lattice parameter and crystallite size of $Co_{1-x}Cu_xFe_2O_4/SiO_2$ as a function of Cu^{2+} content.

detected in XRD patterns due to the low content of amorphous SiO_2. With increasing Cu^{2+} content, the diffraction peak (311) shifts from 35.455° to 35.374° with a small $\Delta\theta$ (0.081°) accompanied by increasing peak intensity and the narrower peak width.

Fig. 3 presents the variation of lattice parameter and crystallite size of $Co_{1-x}Cu_xFe_2O_4$ with Cu^{2+} doping content. The lattice parameter was determined from the X-ray data with MDI Jade 6.5 software using the high-purity silicon powders as a standard sample. It can be seen that the lattice parameter a_o of 8.383 Å for the sample with $x = 0$ is in agreement with the reported value of pure $CoFe_2O_4$.[23] As Cu^{2+} content increases from 0 to 0.3, the lattice parameter a_o slightly increases from 8.383 to 8.389 Å. The increase in lattice parameter can be attributed to the difference in ionic radius of Co^{2+} (0.74 Å) and Cu^{2+} (0.76 Å).[4,24] Furthermore, the average crystallite size, calculated with Scherrer equation is found to increase with increasing Cu^{2+} content (18, 26, 35 and 36 nm for $Co_{1-x}Cu_xFe_2O_4$ with $x = 0$, 0.1, 0.2, and 0.3, respectively). This indicates that the Cu^{2+} doping in $CoFe_2O_4$ NPs favors the grain growth rate during sol–gel preparation process. Similar phenomenon in crystallite size has been also observed by Ashour *et al.* and Dippong *et al.*[25,26]

TEM images of $Co_{1-x}Cu_xFe_2O_4/SiO_2$ samples with $x = 0$ (Fig. 4a) and $x = 0.2$ (Fig. 4b) are shown in Fig. 4. It can be seen that near-spherical Co–Cu ferrites are environed by amorphous SiO_2 without obvious agglomerate. The average sizes are estimated to be 19 ± 5 nm ($x = 0$) and 39 ± 9 nm ($x = 0.2$), respectively, which are consistent with the results determined by XRD. Fig. 4c presents the selective area electron diffraction (SAED) pattern for the $x = 0.2$ sample. The diffraction rings are indexed as lattice plane (111), (220), (311), (400), (511), and (440) for spinel $Co_{0.8}Cu_{0.2}Fe_2O_4$, which is in agreement with the XRD

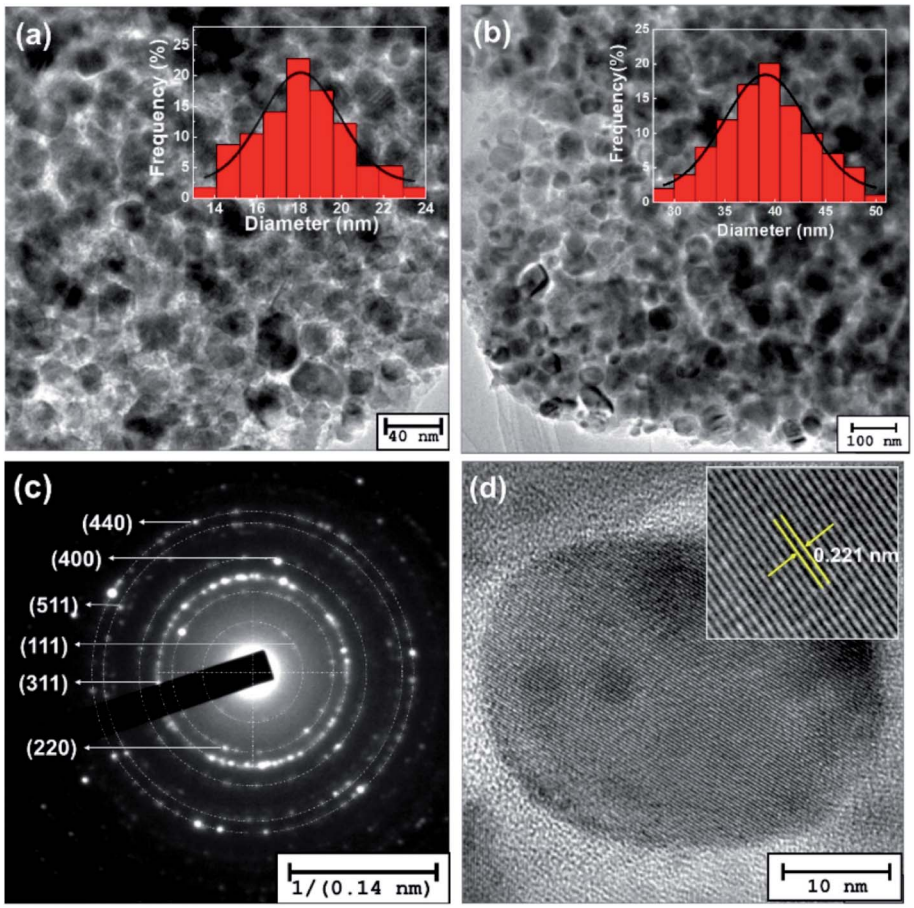

Fig. 4 TEM images of the as-synthesized $Co_{1-x}Cu_xFe_2O_4/SiO_2$ with (a) $x = 0$ and (b) $x = 0.2$. (c) SAED pattern and (d) HRTEM image for $x = 0.2$ sample. Insets in panel (a) and (b) show the average particle size distribution obtained by approximate 50 nanoparticles, respectively.

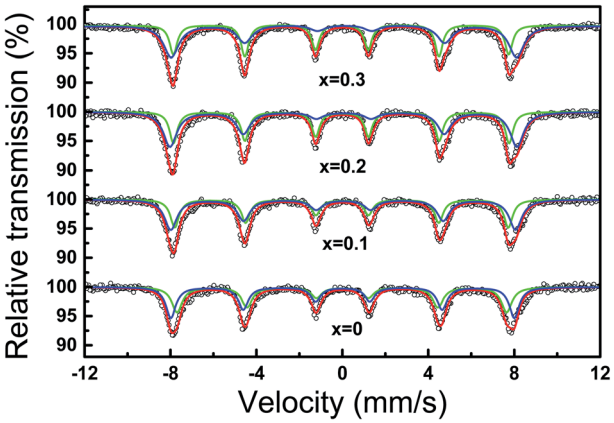

Fig. 5 Mössbauer spectra of $Co_{1-x}Cu_xFe_2O_4/SiO_2$ samples. Symbols represent the experimental data and the continuous line corresponds to the fitting data.

result. The high resolution TEM (HRTEM) image of $Co_{0.8}Cu_{0.2}Fe_2O_4$ in Fig. 4d confirms that the sample is of good crystalline quality, and the clear space fringe with an interplanar spacing of 0.221 nm agrees with the (400) planes of $CoFe_2O_4$NPs.

3.2 Mössbauer spectroscopy

Mössbauer technique serves as one of the most powerful tools for probing the atomic and electronic configuration of Fe atoms, thus, the hyperfine interaction of $Co_{1-x}C_uFe_2O_4$ was investigated through Mössbauer spectra. Fig. 5 shows the experimental Mössbauer spectra and fitting lines of $Co_{1-x}Cu_xFe_2O_4/SiO_2$ with different Cu^{2+} doping contents, and Table 1 presents the correspondingly fitting parameters. These spectra are decomposed into two Zeeman sextets, demonstrating that $Co_{1-x}Cu_xFe_2O_4$ NPs in the obtained samples are ferromagnetically ordered. The values of isomer shifts (IS) are in the range of 0.26–0.40 mm s^{-1}, suggesting that Fe ions in the present $Co_{1-x}Cu_xFe_2O_4$ NPs are in high spin Fe^{3+} charge state. Among two sextets, one with smaller IS and hyperfine field (H_{in}) arises from the tetrahedral Fe^{3+} ions, and the other with larger IS and H_{in} can be ascribed to the octahedral Fe^{3+} ions. It is well known that the value of IS is dependent on s-electron density of Fe^{3+} nucleus. Owing to the larger bond length of Fe^{3+}–O^{2-} at octahedral B sites, the orbital overlapping of Fe^{3+} and O^{2-} is smaller, hence the IS at octahedral B sites is larger than that of tetrahedral A sites. With increasing Cu^{2+} doping content, the IS_A value decreases while the IS_B increases, suggesting that the Cu^{2+} doping behavior can affect the *s*-electron distribution of Fe^{3+} ions at tetrahedral A and octahedral B sites due to Jahn–Teller effect of Cu^{2+} ions.[27]

Among Mössbauer parameters, quadrupole splitting (QS) is related to the crystal symmetry. As seen from Table 1, the value of QS_B gradually increases with Cu^{2+} content, while the values of QS_A do not exhibit a specific tendency. This phenomenon reveals that the local symmetry of octahedral B site Fe^{3+} ions is modified during Cu^{2+} doping process, suggesting that the Cu^{2+} ions preferentially occupied octahedral B sites in the as-prepared Co–Cu ferrites. Owing to Jahn–Teller effect of Cu^{2+} ions at octahedral B sites, they form dsp^2 orbital hybridization and produce strain in $Co_{1-x}Cu_xFe_2O_4$ crystals, inducing the octahedral symmetry to deform slightly without disrupting the lattice symmetry.[28]

As a consequence, hypothesizing that all Cu^{2+} ions locate at octahedral B sites, it is possible to give an estimate of cation distribution for $Co_{1-x}Cu_xFe_2O_4$ NPs as $(Cu_\sigma Fe_{1-\sigma})_A[Co_{1-x-\sigma}Cu_xFe_{1+\sigma}]_B$, where x is Cu^{2+} content and the value of σ can be determined by:

$$\frac{S_A}{S_B} = \frac{{Fe_A}^{3+}}{{Fe_B}^{3+}} = \frac{(1-\sigma)f_A}{(1+\sigma)f_B} \quad (1)$$

Here, assuming the recoilless fraction f_A and f_B to be same, the relative area ratio S_A/S_B thus directly corresponds to the ratio of the number of Fe^{3+} ions at tetrahedral A and octahedral B sites.[27] Based on the Mössbauer fitting data, the ratio S_A/S_B for the $x = 0$ sample is 0.876, thus the cation distribution can be written as $(Co_{0.066}Fe_{0.934})_A\,[Co_{0.934}Fe_{1.066}]_B$, that is to say, 93.4% of Co^{2+} ions resides at octahedral B sites. Sawatzky *et al.*[29] reported that the ratio of octahedral Co^{2+} ions in $CoFe_2O_4$ depended on the heat treatment. They estimated that 96% and 79% of Co^{2+} ions presented in the slowly cooled and quenched $CoFe_2O_4$ NPs, respectively. When Cu^{2+} ions is doped in $CoFe_2O_4$, the ratio of S_A/S_B for $x = 0.1$ sample becomes 0.792. The cation distribution is represented as $(Co_{0.116}Fe_{0.884})_A[Co_{0.784}Cu_{0.1}Fe_{1.116}]_B$, demonstrating that Cu^{2+} doping results in the relocation of small amount of Co^{2+} from B to A sites concomitantly with some Fe^{3+} ions migrated from A to B sites, although Cu^{2+} ions locate at the octahedral B sites. Further

Table 1 Mössbauer parameters of $Co_{1-x}Cu_xFe_2O_4/SiO_2$ samples[a]

Sample	Component	IS (mm s^{-1})	QS (mm s^{-1})	H_{in} (T)	FWHM (mm s^{-1})	S (%)	S_A/S_B
$x = 0$	Sextet (A)	0.300 ± 0.004	0.027 ± 0.008	47.6 ± 1.1	0.296 ± 0.012	46.7	0.876
	Sextet (B)	0.324 ± 0.003	0.007 ± 0.002	49.6 ± 0.9	0.279 ± 0.011	53.3	
$x = 0.1$	Sextet (A)	0.292 ± 0.003	0.022 ± 0.004	48.0 ± 0.8	0.248 ± 0.010	44.2	0.792
	Sextet (B)	0.346 ± 0.007	0.014 ± 0.003	49.8 ± 0.8	0.326 ± 0.021	55.8	
$x = 0.2$	Sextet (A)	0.280 ± 0.005	0.037 ± 0.001	48.4 ± 0.7	0.222 ± 0.007	43.8	0.779
	Sextet (B)	0.369 ± 0.010	0.023 ± 0.003	50.0 ± 0.8	0.383 ± 0.011	56.2	
$x = 0.3$	Sextet (A)	0.269 ± 0.006	0.039 ± 0.002	48.4 ± 0.6	0.217 ± 0.013	43.7	0.776
	Sextet (B)	0.399 ± 0.011	0.039 ± 0.003	49.8 ± 0.9	0.434 ± 0.011	56.3	

[a] IS = isomer shift; QS = quadruple split, H_{in} = hyperfine field, S = relative absorption area, FWHM = the half width at half maximum.

increasing Cu^{2+} content to 0.2 and 0.3, it is found that the concentration of Fe^{3+} ion in A and B sites almost unchanged ($S_A/S_B = 0.779$ for $x = 0.2$ and 0.776 for $x = 0.3$ sample), revealing that Cu^{2+} ions only replace octahedral Co^{2+} ions, and make no effect on Fe^{3+} distribution. The cation distribution can be written as $(Co_{0.124}Fe_{0.876})_A\ [Co_{0.676}Cu_{0.2}Fe_{1.124}]_B$ for the sample with $x = 0.2$, and $(Co_{0.126}Fe_{0.874})_A\ [Co_{0.574}Cu_{0.3}Fe_{1.126}]_B$ for the sample with $x = 0.3$.

From the 7th column of Table 1, we find that the half width at half maximum (FWHM) of A and B lines varies with Cu^{2+} content. In cubic spinel lattice, each A-site Fe^{3+} ion is surrounded by 12 nearest B-site ions neighbors and each B-site Fe^{3+} ion is surrounded by 6 nearest A-site ions neighbors, thus B-site Fe^{3+} is more sensitive to the change in the surrounding cation distribution than the A-site Fe^{3+} ions. According to the cation distribution, for the sample with $x = 0$, each Fe^{3+} ion in A and B sites is surrounded by approximately 6 nearest Fe^{3+} ions, therefore, the line width is comparable but relatively narrow. When Cu^{2+} ions are doped in $CoFe_2O_4$ lattice, some Fe^{3+} ions migrate from A to B sites, hence the A site Fe^{3+} ions get more nearest Fe_B^{3+} neighbors. This leads to a reduction in the total super-exchange strength of B-site Fe^{3+} ions while an increase in A-site Fe^{3+} ions.[30] Consequently, broadened B line and narrowed A line are observed in Co–Cu ferrite. In addition, Table 1 also presents the same increasing trend of the hyperfine field (H_{in}) for tetrahedral A and octahedral B sites with increasing Cu^{2+} content. The weighted average values of H_{in} are 48.7, 49.0, 49.3, and 49.2 T for the $Co_{1-x}Cu_xFe_2O_4$ with $x = 0$, 0.1, 0.2, and 0.3, respectively. The increase in H_{in} can be attributed to the increasing crystallite size, since the fluctuation of magnetization vectors close to easy direction of magnetization can give rise to a size dependent magnetic hyperfine field.[31]

3.3 Magnetic properties analysis

Fig. 6a shows the magnetic hysteresis loops of $Co_{1-x}Cu_xFe_2O_4/SiO_2$ samples measured at room temperature. Clearly, these loops show the typical characteristics of ferromagnetic materials. At the applied field intensity (15 kOe), saturation state cannot be reached yet, thus the saturation magnetization M_s was estimated by fitting the high-field part of the magnetization curves using the relation $M = M_s \times \left(1 - \frac{a}{H} - \frac{b}{H^2}\right)$, here H is the field strength, a and b are constant determined by the fitting procedure.[32] The fitted M_s and the measured coercivity H_c are plotted as functions of Cu^{2+} content x in Fig. 6b. The M_s for the pure $CoFe_2O_4$ is 24.7 emu g^{-1}, which is close to the reported value for 10–15 nm $CoFe_2O_4/SiO_2$ (30–50% SiO_2) prepared sol–gel method.[19] The low M_s for pure $CoFe_2O_4$ sample can be attributed to the existence of amorphous SiO_2 matrix, which modifies the magnetic behavior through minimizing the particle interactions between ferrite particles.[33,34] The value of M_s first increases to 34.3 emu g^{-1} when Cu^{2+} content is 0.1, and then reduces to 27.1 emu g^{-1} as Cu^{2+} content further increases to 0.3. Two factors are possibly responsible for the higher M_s values for Cu-doping $CoFe_2O_4$ comparing with pure $CoFe_2O_4$. For $x = 0.1$ sample, the Mössbauer analysis indicates that doping Cu^{2+} ions with magnetic moment 1 μ_B results in the migration of Fe^{3+} ions from tetrahedral A to octahedral B sites. This behavior leads to the magnetization of the octahedral B sites and hence the M_s increases.[35] For the samples with $x = 0.2$ and 0.3, more Cu^{2+} ions occupied B-sites decreases the B-sublattice magnetization, thereby the enhanced M_s can be attributed to the increasing crystallite sizes with Cu^{2+} content. Noted that the M_s of 34.3 emu g^{-1} for the $x = 0.1$ sample is about 38.9% larger than pure $CoFe_2O_4$.

Considering the Neel' two sub-lattice collinear model of ferrimagnetism, the magnetic moment η_B^{Neel} per unit formula in Bohr magneton can be estimated by $\eta_B^{Neel} = M_B(x) - M_A(x)$.[36] Assuming the magnetic moment of Fe^{3+}, Co^{2+} and Cu^{2+} to be 5, 3 and 1 μ_B, respectively, then using the obtained cation distribution from Mössbauer analysis, the magnetic moments η_B^{Neel} are calculated and summarized in Table 2. Meanwhile, Table 2 also provides the magnetic moment η_B^{obs} determined by the fitted M_s using the following formula:[37] $\eta_B^{obs} = (M_w \times M_s)/5585$, where M_w is the molecular weight of the ferrite. As Table 2 indicates, the calculated values of η_B^{obs} are smaller than that of η_B^{Neel}, which suggests Neel's collinear model is not suitable for the obtained samples. Moreover, there is a significant canted spin arrangement in B-sites, which enhances the B–B interaction and in turn decreases the A–B interaction. According to the Yafet and Kittel's three sublattice model, the spin-canting angle θ_{YK} (Yafet–Kittle angle) is calculated by:[38]

$$\cos\theta_{YK} = \frac{\eta_B^{obs} + M_A(x)}{M_B(x)} \quad (2)$$

The results are given in Table 2. It should be noted that the values of θ_{YK} is 38.6° for $x = 0.1$ sample, comparable to the

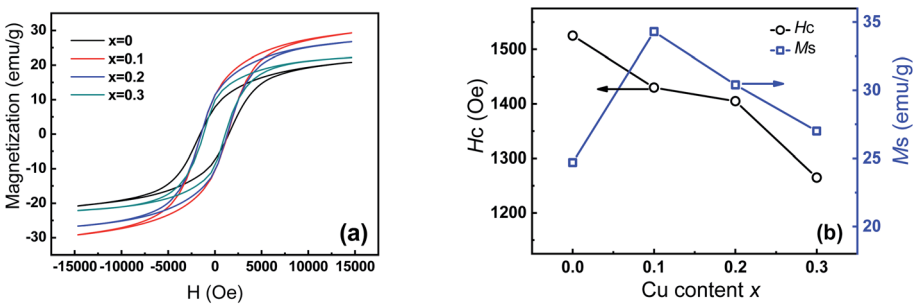

Fig. 6 (a) Hysteresis loops of $Co_{1-x}Cu_xFe_2O_4/SiO_2$, (b) plot of M_s and H_c of samples as a function of Cu^{2+} content.

Table 2 Magnetic parameters of $Co_{1-x}Cu_xFe_2O_4/SiO_2$ at room temperature

Sample	M_s (emu g^{-1})	M_r (emu g^{-1})	H_c (Oe)	η_B^{obs} (μ_B)	η_B^{Neel} (μ_B)	θ_{YK} (degree)
$x = 0$	24.7	7.6	1525	1.48	3.26	38.6
$x = 0.1$	34.3	11.1	1430	2.06	3.37	33.6
$X = 0.2$	30.4	10.8	1405	1.83	3.10	33.1
$X = 0.3$	27.1	9.35	1265	1.63	2.91	33.4

reported value for $CoFe_2O_4/SiO_2$ with 30% silica in ref. 39. However, the θ_{YK} decreases to $\sim 33^\circ$ for Cu-doping ferrites (Table 2), which indicates the presence of Cu^{2+} ions at B sites reduces the degree of spin canting. Using high field Mössbauer spectra, Peddis *et al.*[39,40] confirmed that the spin canting mainly located in the octahedral B sites. Owing to the high anisotropy energy of Co^{2+} ions,[41] the non-collinear canting spin mainly occurs in B-site Fe^{3+} magnetic moment.[42,43] The similar θ_{YK} values observed in as-prepared $Co_{1-x}Cu_xFe_2O_4$ with 18–36 nm sizes indicate that the spin canting is not a surface phenomenon but an effect throughout the volume of the particles, including surface spin and core spin.[41]

On the other hand, the coercivity H_c decreases continuously from 1525 to 1265 Oe as Cu^{2+} doping content increases from 0 to 0.3. The change in H_c with Cu^{2+} content may be related to crystallite size, cation distribution, and magneto crystalline anisotropy constant. It is well known that the H_c of magnetic particle with single domain should increase with crystallite size in principle. In the present case, the average crystallite sizes of $Co_{1-x}Cu_xFe_2O_4$ NPs are lower than the single domain critical size (40 nm) of $CoFe_2O_4$ NPs. Therefore, the decrease in H_c should be attributed to the cation distribution and magneto-crystalline anisotropy constant. Since Co^{2+} ion at octahedral B site has larger anisotropy ($+850 \times 10^{-24}$ J per ion) than that at tetrahedral A site (-79×10^{-24} J per ion),[44] the octahedral Co^{2+} ions can be responsible for the high magneto-crystalline anisotropy of $CoFe_2O_4$.[45,46] The replacement of octahedral Co^{2+} by Cu^{2+} ion results in the reduction in the percentage of Co^{2+} in B sites, and thus decreases the anisotropy constant.

4. Conclusions

To summarize, we have studied the effect of Cu^{2+} doping content on the microstructural and magnetic properties of $Co_{1-x}Cu_xFe_2O_4/SiO_2$ ($0 \le x \le 0.3$) nanocomposites. Although all the obtained $Co_{1-x}Cu_xFe_2O_4$ NPs have cubic spinel structure, the substitution of Cu^{2+} for Co^{2+} ions can bring change in the crystallite size, cation distribution, and magnetic properties. The crystallite size increases with Cu^{2+} doping content. The preferred occupancy of Cu^{2+} ions at octahedral B sites results in slight deformation of octahedral symmetry and Fe^{3+} ions migration from tetrahedral A to octahedral B sites. Moreover, the values of M_s and H_c are strongly dependent on Cu^{2+} doping content, which can be attributed to the cation migration between both sublattices (A and B). The relatively large spin-canting angle θ_{YK} reveals that the spin canting mainly occurs in the octahedral Fe^{3+} throughout the particles. The results suggest that the Cu^{2+} doping content in $Co_{1-x}Cu_xFe_2O_4$ NPs can play an important role in tuning their physical properties, which may be of great significance in to exploit novel applications in high density information storage, electronic devices and biomedicine.

Conflicts of interest

There are no conflicts to declare.

Acknowledgements

This work was supported by the National Natural Science Foundation of China (Nos. 21371071), Foundation of Science and Technology of Jilin, China (Grant No. 201205075).

References

1 Z. T. Zhang, A. J. Rondinone, J. X. Ma, J. Shen and S. Dai, Morphologically Templated Growth of Aligned Spinel $CoFe_2O_4$ Nanorods, *Adv. Mater.*, 2005, **17**(11), 1415–1419.
2 L. Demir, U. Perisanoglu and M. Sahin, Investigating XRF parameters and valance electronic structure of the Co, Ni, and Cu spinel ferrite, *Ceram. Int.*, 2019, **45**, 7748–7753.
3 M. Zhang,F, Z. ,Y. Yang, T. An, W. Qu, H. Li, J. Zhang and N. Li, Catalytic activity of ferrates ($NiFe_2O_4$, $ZnFe_2O_4$ and $CoFe_2O_4$) on the thermal decomposition of ammonium perchlorate, *Propell., Explos., Pyrot.*, 2020, **45**(3), 463–471.
4 M. Sundararajan and L. J. Kennedy, Photocatalytic removal of rhodamine B under irradiation of visible light using $Co_{1-x}Cu_xFe_2O_4$ ($0\le x\le 0.5$) nanoparticles, *J. Environ. Chem. Eng.*, 2017, **5**(4), 4075–4092.
5 B. Li, H. T. Fan, X. Xing, Y. Yang, C. C. Wang and D. F. Qiu, Triple functions nanocomposites of porous silica-$CoFe_2O_4$-MWCNTs as carrier for pH-sensitive anti-cancer drugs controlled delivery, *Dalton Trans.*, 2017, **46**, 14831–14838.
6 J. Yang, Y. Chen, Y. H. Li and X. B. Yin, Magnetic resonance imaging-guided multi-drug chemotherapy and photothermal synergistic therapy with ph and nir-stimulation release, *ACS Appl. Mater. Interfaces*, 2017, **9**(27), 22278–22288.
7 T. Walther, U. Straube, R. Koferstein and S. G. Ebbinghaus, Hysteretic magnetoelectric behavior of $CoFe_2O_4$-$BaTiO_3$ composites prepared by reductive sintering and reoxidation, *J. Mater. Chem. C*, 2016, **4**, 4792–4799.
8 C. Venkateshwarlu and D. Ravinder, Thermoelectric power studies of Cu-Co ferrites, *J. Alloy Compd.*, 2006, **426**, 4–6.

9 T. Tatarchuk, M. Bououdina, W. Macyk, O. Shyichuk, N. Paliychuk, I. Yaremiy, B. Al-Najar and M. Pacia, Structural, optical, and magnetic properties of Zn-doped $CoFe_2O_4$ nanoparticles, *Nanoscale Res. Lett.*, 2017, **12**(1–11), 141.

10 G. Xi and Y. Xi, Effects on magnetic properties of different metal ions substitution cobalt ferrites synthesis by sol–gel auto-combustion route using used batteries, *Mater. Lett.*, 2016, **164**, 444–448.

11 N. Sanpo, C. C. Berndt, C. Wen and J. Wang, Transition metal-substituted cobalt ferrite nanoparticles for biomedical applications, *Acta Biomater.*, 2013, **9**(3), 5830–5837.

12 J. Balavijayalakshmi, N. Suriyanarayanan and R. Jayapraksah, Influence of copper on the magnetic properties of cobalt ferrite nanoparticles, *Mater. Lett.*, 2012, **81**, 52–54.

13 R. A. Mecurrie, *Ferromagnetic material structure and properties*, Academic Press, London, 1994.

14 M. Kucera and P. Brom, Magneto-optical properties of nano-crystalline cubic and tetragonal copper ferrite thin films, *J. Appl. Phys.*, 2018, **117**, 17B738.

15 T. Muthukumaran and J. Philip, Synthesis of water dispersible phosphate capped $CoFe_2O_4$ nanoparticles and its applications in efficient organic dye removal, *Colloid. Surface. A*, 2021, **610**, 125755.

16 T. Muthukumaran and J. Philip, A facile approach to synthesis of cobalt ferrite nanoparticles with a uniform ultrathin layer of silicon carbide for organic dye removal, *J. Mol. Liq.*, 2020, **317**(1–14), 114110.

17 M. Gharagozlou, B. Ramezanzadeh and Z. Baradaran, Synthesize and characterization of a novel anticorrosive cobalt ferrite nanoparticles dispersed in silica matrix ($CoFe_2O_4$-SiO_2) to improve the corrosion protection performance of epoxy coating, *Appl. Surf. Sci.*, 2016, **377**, 86–98.

18 Z. S. Piskuła, P. Skokowski, T. Tolinski, M. Zielinski, P. Kirszensztejn and W. Nowicki, Structure, magnetic and catalytic properties of SiO_2-MFe_2O_4 (M =Mn, Co, Ni, Cu) nanocomposites and their syntheses by a modified sol–gel method, *Mater. Chem. Phys.*, 2019, **235**, 121731.

19 T. Dippong, O. Cadar, E. A. Levei, I. Bibicu, L. Diamandescu, C. Leostean, M. Lazar, G. Borodi and L. B. Tudoran, Structure and magnetic properties of $CoFe_2O_4$/SiO_2 nanocomposites obtained by sol–gel and post annealing pathways, *Ceram. Int.*, 2017, **43**, 2113–2122.

20 J. Hua, Y. Liu, L. Wang, M. Feng, J. Zhao and H. Li, Mössbauer studies on Mn substituted $CoFe_2O_4$/SiO_2 nanocomposites synthesized by sol–gel method, *J. Magn. Magn. Mater.*, 2016, **402**, 166–171.

21 K. Nadeem, T. Traussnig, I. Letofsky-Papst, H. Krenn and U. Brossmann, Sol–gel synthesis and characterization of single-phase Ni ferrite nanoparticles dispersed in SiO_2 matrix, *J. Alloy. Compd.*, 2010, **493**, 385–390.

22 S. Rohilla, S. Kumar, P. Aghamkar, S. Sunder and A. Agarwal, Investigations on structural and magnetic properties of cobalt ferrite/silica nanocomposites prepared by the coprecipitation method, *J. Magn. Magn. Mater.*, 2011, **323**, 897–902.

23 Y. Tang, X. Wang, Q. Zhang, Y. Li and H. Wang, Solvothermal synthesis of $Co_{1-x}Ni_xFe_2O_4$ and its application in ammonia vapors detection Progress in natural science, *Mater. Inter.*, 2012, **22**, 53–58.

24 C. C. Naik, S. K. Gaonkar, I. Furtado and A. V. Salker, Effect of Cu^{2+} substitution on structural, magnetic and dielectric properties of cobalt ferrite with its enhanced antimicrobial property, *J. Mater. Sci-Mater. El.*, 2018, **29**, 14746–14761.

25 A. H. Ashour, A. I. El-Batal, M. I. A. Abde Maksoud, G. S. El-Sayyad, S. Labib, E. Abdeltwab and M. M. El-Okr, Antimicrobial activity of metal-substituted cobalt ferrite nanoparticles synthesized by sol–gel technique, *Particuology*, 2018, **40**, 141–151.

26 T. Dipponga, I. G. Deacb, O. Cadarc, E. A. Leveic and I. Peteand, Impact of Cu^{2+} substitution by Co^{2+} on the structural and magnetic properties of $CuFe_2O_4$ synthesized by sol–gel route, *Mater. Charact.*, 2020, **163**, 110248.

27 B. K. Chatterjee, K. Bhattacharjee, A. Dey, C. K. Ghosha and K. K. Chattopadhyay, Influence of spherical assembly of copper ferrite nanoparticles on magnetic properties: orientation of magnetic easy axis, *Dalton Trans.*, 2014, **43**, 7930–7944.

28 A. B. Naik, S. R. Sawant, S. A. Patil and J. I. Powar, On the variation of a.c. susceptibility with temperature for some Cu-Li ferrites,Bull, *Mater. Sci.*, 1988, **11**(4), 315–318.

29 G. A. Sawatzky, F. V. D. Woude and A. H. Morrish, Cation distributions in octahedral and tetrahedral sites of the ferromagnetic spinel $CoFe_2O_4$, *J. Appl. Phys.*, 1968, **39**, 1204–1205.

30 G. A. Sawatzkyt, F. D. W. Van and A. H. Morrish, Mössbauer study of several ferrimagnetic spinels, *Phys. Rev.*, 1969, **187**(2), 747–757.

31 K. M. Batoo, D. Salah, G. Kumar, A. Kumar, M. Singh, M. A. El-sadek, F. A. Mir, A. Imran and D. A. Jameel, Hyperfine interaction and tuning of magnetic anisotropy of Cu doped $CoFe_2O_4$ ferrite nanoparticles, *J. Magn. Magn. Mater.*, 2016, **411**, 91–97.

32 A. H. Morrish, *The physical principles of magnetism*, Wiley, New York, 1965.

33 V. Blanco-Gutiérrez, M. Virumbrales, R. Saez-Puche and M. J. Torralvo-Fernández, Superparamagnetic Behavior of MFe_2O_4 Nanoparticles and MFe_2O_4/SiO_2 Composites (M: Co, Ni), *J. Phys. Chem. C*, 2013, **117**(40), 20927–20935.

34 M. Virumbrales, R. Saez-Puche, M. J. Torralvo and V. Blanco-Gutierrez, Mesoporous silica matrix as a tool for minimizing dipolar interactions in $NiFe_2O_4$ and $ZnFe_2O_4$ nanoparticles, *Nanomaterials*, 2017, **7**, 151.

35 M. Hashim, Alimuddin, S. Kumar, B. H. Koo, S. E. Shirsath, E. M. Mohammed, J. Shah, R. K. Kotnala, H. K. Choi, H. Chung and R. Kumar, Structural, electric and magnetic properties of Co-Cu ferrite nanoparticles, *J. Alloy. Compd.*, 2012, **518**, 11–18.

36 L. Néel, Magnetic properties of ferrites: ferrimagnetism and antiferromagnetism, *Ann. Phys. Paris.*, 1948, 137–198.

37 B. G. Toksha, S. E. Shirsath, M. L. Mane, S. M. Patange, S. S. Jadhav and K. M. Jadhav, Autocombustion high-temperature synthesis, structural, and magnetic properties of $CoCr_xFe_{2-x}O_4$ ($0 \leq x \leq 1.0$), *J. Phys. Chem. C*, 2011, **115**, 20905–20912.

38 Y. Yafet and C. Kittel, Antiferromagnetic arrangements in ferrites, *Phys. Rev.*, 1952, **87**, 290.

39 D. Peddis, M. V. Mansilla, S. Morup, C. Cannas, A. Musinu, G. Piccaluga, F. Orazio, F. Lucari and D. Fiorani, Spin-canting and magnetic anisotropy in ultrasmall $CoFe_2O_4$ nanoparticles, *J. Phys. Chem. B*, 2008, **112**, 8507.

40 D. Peddis, C. Cannas, G. Piccaluga, E. Agostinelli and D. Fiorani, Spin-glass-like freezing and enhanced magnetization in ultra-small $CoFe_2O_4$ nanoparticles, *Nanotechnology*, 2010, **21**(1–10), 125705.

41 C. Cannas, A. Musinu, G. Piccaluga, D. Fiorani, D. Peddis, H. K. Rasmussen and S. Mørup, Magnetic properties of cobalt ferrite-silica nanocomposites prepared by a sol–gel autocombustion technique, *J. Chem. Phys.*, 2006, **125**(535), 164714.

42 C. Bellitto, E. M. Bauer and G. Righini, On the crystalstructures and magnetism of some hybrid organic–inorganic metal organophosphonates, *Inorg. Chim. Acta*, 2008, **361**, 3785–3799.

43 D. Peddis, N. Yaacoub, M. Ferretti, A. Martinelli, G. Piccaluga, A. Musinu, C. Cannas, G. Navarra, J. M. Greneche and D. Fiorani, Cationic distribution and spin canting in $CoFe_2O_4$ nanoparticles, *J. Phys.: Condens. Matter*, 2011, **23**, 426004.

44 H. Y. Zhang, B. X. Gu, H. R. Zhai, Y. Z. Miao, S. Y. Zhang and H. B. Huang, Anisotropy and Faraday effect in Co spinel ferrite films, *J. Appl. Phys.*, 1994, **75**, 7099–7101.

45 J. F. Hochepied, Ph. Sainctavit and M. P. Pileni, X-ray absorption spectra and X-ray magnetic circular dichroism studies at Fe and Co $L_{2,3}$ edges of mixed cobalt-zinc ferrite nanoparticles: cationic repartition, magnetic structure and hysteresis cycles, *J. Magn. Magn. Mater.*, 2001, **231**, 315–322.

46 A. A. Ati, Z. Othaman and A. Samavati, Influence of cobalt on structural and magnetic properties of nickel ferrite nanoparticles, *J. Mol. Struct.*, 2013, **1052**, 177–182.